Analysis and Design of Multifrequency Compensation Strategy for Wide Misalignment Tolerance in Inductive Power Transfer Systems

Zirui Yao, *Student Member, IEEE*, Shiying Luo, Zhuhaobo Zhang, *Student Member, IEEE*, Guanxi Li, Xuan Wei, *Student Member, IEEE*, Xiangwei Shen, Ni Zhang, Philip T. Krein, *Fellow, IEEE*, and Hao Ma, *Senior Member, IEEE*

***Abstract*—In inductive power transfer systems, misalignment can lead to inconsistent output power. In this article, a topology based on a primary-side detuned multifrequency compensation circuit is proposed to provide consistent output over a wide misalignment range. This topology exhibits multiple intersecting power versus coupling coefficient curves given multiple switching frequencies. The coupling range, and associated misalignment range, can be extended without increasing power and current variability by changing the switching frequency strategically at curve intersections. Parameter design and selection of the number of switching frequencies are presented. Fundamental relationships between power variation and coupling range are established. With this approach, a choice of two suitable switching frequencies changes output power by only 10% over a coupling coefficient range from 0.14 to 0.35. Three frequencies can support lower power variation or a wider coupling range. Primary current at low coupling is lower with the strategy than for conventional alternatives because reactive power can be limited. A 1.5 kW prototype has been prepared to verify the topology. The prototype confirms a power variation of 10% over a coupling coefficient range from 0.14 to 0.35 with two frequencies. With three frequencies, power variation drops to 6.7% over the same coupling range.**

Manuscript received 14 February 2023; revised 5 May 2023; accepted 2 June 2023. Date of publication 19 June 2023; date of current version 28 July 2023. This work was supported in part by the National Natural Science Foundation of China under Grants 51577171 and 51977190, and in part by the Zhejiang University/University of Illinois at Urbana-Champaign Institute, led by Principal Supervisors Hao Ma and Philip T. Krein. Recommended for publication by Associate Editor S. Mekhilef. *(Corresponding author: Hao Ma.)*

Zirui Yao, Zhuhaobo Zhang, and Hao Ma are with the College of Electrical Engineering, Zhejiang University, Hangzhou 310027, China, and also with the Zhejiang University/University of Illinois at Urbana-Champaign Institute, Haining 314400, China (e-mail: 11810009@zju.edu.cn; zzhbpain@163.com; mahao@zju.edu.cn).

Shiying Luo, Guanxi Li, Xuan Wei, and Xiangwei Shen are with the College of Electrical Engineering, Zhejiang University, Hangzhou 310027, China (e-mail: luoshiying0318@qq.com; 270342773@qq.com; 1029244098@qq.com; 12010014@zju.edu.cn).

Ni Zhang is with the College of Information Engineering, Zhejiang University of Technology, Hangzhou 310027, China (e-mail: zn@zjut.edu.cn).

Philip T. Krein is with the College of Electrical Engineering, Zhejiang University, Hangzhou 310027, China, also with the Zhejiang University/University of Illinois at Urbana-Champaign Institute, Haining 314400, China, and also with the University of Illinois at Urbana-Champaign, Urbana, IL 61820 USA (e-mail: krein@illinois.edu).

Color versions of one or more figures in this article are available at https://doi.org/10.1109/TPEL.2023.3287352.

Digital Object Identifier 10.1109/TPEL.2023.3287352

***Index Terms*—Detuned primary, inductive power transfer (IPT), misalignment tolerance, multifrequency compensation, resonant conversion.**

I. Introduction

INDUCTIVE power transfer (IPT) systems can transfer energy to loads through magnetic coupling [1], [2], [3], [4], [5]. Compared to conventional wire-connected electrical transfer systems, IPT systems are appealing for electric ferries and other large systems because of contactless performance metrics [6]. In IPT-charged electric ferries, for instance, relative positions of primary and secondary coils change in real time owing to water motion. The coupling coefficient and transmission power will be affected continuously by misalignment [6]. Other large systems such as IPT for long-haul trucks or construction loaders are less dynamic but still subject to uncertain misalignment [3], [4], [5]. In any such system, improved performance is needed across high coupling and low coupling. Although internal charge regulation can maintain the charging voltage or current, the power limit is affected by misalignment. Wide power variation with misalignment will increase charging time, impose higher component ratings, and decrease system efficiency [7]. A practical IPT system will benefit if it can maintain consistent output power over a useful misalignment range.

In this article, a primary-side detuned multifrequency compensation structure is proposed to enhance output characteristics and keep them consistent over a wide misalignment range. Multiple separate switching frequencies are employed, and the proper frequency is selected to enforce a limited input impedance range to maintain consistent output power. The multifrequency approach here leads to multiple intersecting power versus coupling coefficient curves. Based on these curves, the control strategy changes the switching frequency to extend the misalignment range given constrained power variation. The input impedance angle range follows a similar level of variation. This is used to advantage to keep reactive input low and reduce the primary current at low coupling. The topology can ensure zero voltage switching (ZVS) over the allowed range of coupling conditions.

Multifrequency methods are known in IPT systems and have been used in multiport applications. Multi-inverter parallel operation was presented in [8], [9], and [10] to transfer power

from multiple primary coils to independent loads. In [11], [12], and [13], a hybrid modulation pulsewidth modulation (PWM) control method was proposed to generate different frequencies to supply energy to multiple receivers. Hard switching and a relatively high switching frequency affected system efficiency. A selective power transfer method with multiple receivers [14] has been proposed to achieve controllable power division by changing the switching frequency to match different secondary resonant frequencies. A two-phase orthogonal coil structure with a two-frequency phase-shifted control method was presented in [15] to realize targeted power distribution between loads with misalignment, but the operation improved only for rotational misalignment. In [16], a two-frequency hybrid compensation topology integrates series–series (S-S) compensation and *LCC*-S compensation for the fundamental and third-order harmonic voltages of a full-bridge inverter to compensate misalignment. The coupling coefficient needed to be high to achieve target output power at the two frequencies because the third harmonic voltage is one-third of the fundamental voltage.

The system described in this article is different. It uses a single IPT stage without extra inverters or coils and employs multiple switching frequencies to manage output power and input current variation over a substantial misalignment range. Although it requires multiple resonant tuning tanks, it achieves consistent performance for a single power transfer port.

IPT systems are characterized by loosely coupled transformers. Many prior methods sought to enhance coupling rather than adapting to it. Flux pipe magnetic couplers [17], double-D polarized couplers [18], double-D quadrature configurations [18], quadrature coils [19], and bipolar pads [20] have been proposed to extend the misalignment range. In [21], parameters of the transformer that include coil shapes, coil diameters, and ferrite arrangements have been used to optimize the coupling coefficient. A cubic-magnetic coupler was presented in [22] based on concentrated magnetic flux. These methods can alleviate the impact of decreased coupling, but output power is still affected. In some methods, extra coils were added to improve misalignment performance [23], [24], [25]. Although the output power can be relatively constant, added coils introduce extra loss, volume, and cost.

Topologies such as T-type [26] and X-type circuits [27] based on detuned compensation structures have been proposed to reduce output power variation with misalignment. The transferred power changed by as little as 20% with misalignment in these cases. In [28], a reconfigurable topology used ac switches to apply two power-transfer coupling-coefficient curves. The output power changed by only 10% over a coupling coefficient range from 0.10 to 0.25, but the added ac switches and controllers limit the ability to scale the approach to higher power. Hybrid structures constructed with conventional series compensation circuits and *LCC* compensation circuits were proposed in [29] and [30]. In those methods, the structure of the magnetic coupler and performance in certain directions are limited because of decoupling requirements among compensation circuits.

Converter control that includes pulse frequency modulation (PFM) [31], [32] and PWM [33], [34] has been proposed to improve misalignment performance. For PFM, primary current increases as coupling coefficient decreases [31], [32]. PWM and active rectification are used to maintain consistent power, but hard switching is employed for the inverter and rectifier [33]. In [34], a control method that integrates PWM with frequency control is proposed to achieve soft switching over the allowed range of operating conditions. This method will increase input impedance angle and reactive power even with soft-switching operation.

The proposed system seeks to address disadvantages of ac switch approaches and control limits. By making use of switching frequency selection, it adapts to misalignment. Compared to conventional single-frequency compensation topologies, the proposed topology extends the useful misalignment range while enforcing a power variation limit. The use of discrete switching frequencies helps to avoid frequency bifurcation [35] compared to continuous frequency control, and the system can avoid chattering near the coupling intersection point by encompassing a hysteresis control in its frequency selection strategy.

The rest of this article is organized as follows. The proposed primary detuned multifrequency compensation topology is analyzed in Section II. Output characteristics of the proposed topology for different numbers of switching frequencies and misalignment performance comparisons are described in Section III. Parameter design and selection of the number of switching frequencies are provided in Section IV. Experimental results from a 1.5 kW prototype IPT system and comparisons to other methods are presented in Section V. Finally, Section VI concludes the article.

II. Analysis of the Proposed Primary Detuned Multifrequency Compensation Topology

The proposed multifrequency IPT system is shown in Fig. 1, with an equivalent circuit. L_p and L_s are self-inductances of the primary and secondary coils. The primary and secondary resonant circuits consist of one series *LC* resonant tank and *n*–1 parallel *LCC* resonant tanks, and have *n* resonant frequencies. There is one resonant tank for each potential choice of switching frequency. When $n = 1$, the circuit is a conventional S-S compensation topology. The ideal input-to-output voltage gain versus frequency for the resonant set is shown in Fig. 2. The network acts as a multiple bandpass filter, and when the switching frequency matches any of the multifrequency network resonances, the ideal voltage gain is 1. An important consideration is that component quality factor Q will enter into practical performance. Each additional tank introduces its own series resistance, reducing the overall voltage gain. The dc source V_{in} supplies a MOSFET bridge (S_1, S_2, S_3, S_4). The secondary resonant circuit drives load R_o through rectifier bridge D_1, D_2, D_3, D_4.

Fundamental harmonic analysis is used here. The simplified ideal circuit in Fig. 1(b) defines

$$\begin{cases} U_{AB} = \frac{2\sqrt{2}}{\pi} V_{\text{in}},\ U_{CD} = \frac{2\sqrt{2}}{\pi} V_{\text{out}} \\ M = k\sqrt{L_p L_s},\ R_{\text{eq}} = \frac{8}{\pi^2} R_o \end{cases} \tag{1}$$

where U_{AB} and U_{CD} are the rms values of first-harmonic input and output voltages, respectively; R_{eq} is the ac equivalent load; k

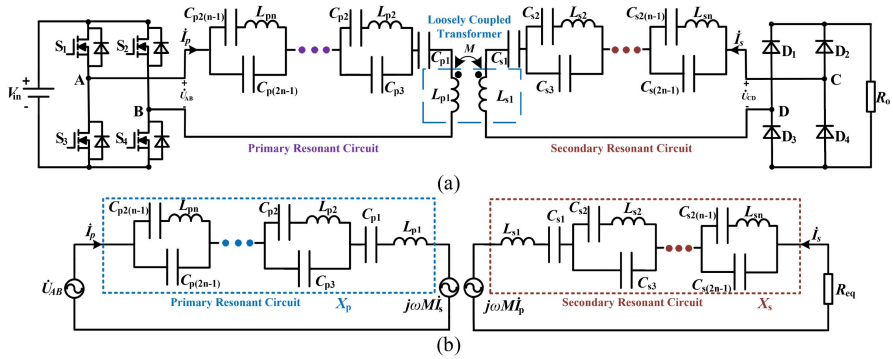

Fig. 1. Proposed multifrequency compensation IPT system. (a) Proposed topology. (b) Simplified equivalent circuit.

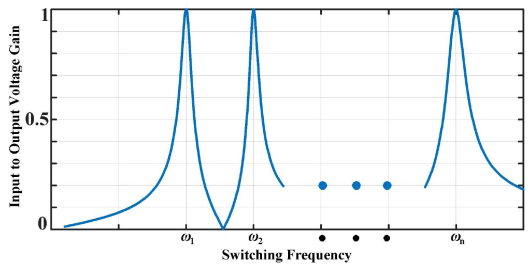

Fig. 2. Input-to-output voltage gain curve versus frequency for multifrequency resonant network.

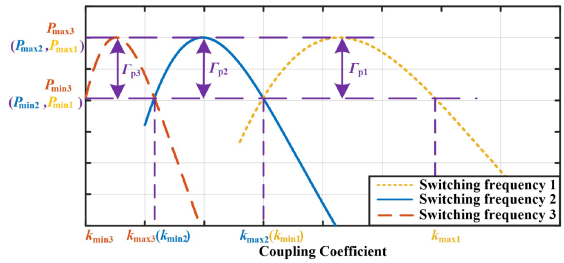

Fig. 3. Output characteristics at three switching frequencies ($f_1 < f_2 < f_3$) and the same power variation with a constant X_{pi}.

is the transformer coupling coefficient, and wider misalignment between the coils will reduce it.

For a given radian frequency ω, the coupled voltage relationships are

$$\begin{cases} \dot{U}_{AB} = jX_p\dot{I}_p + j\omega M\dot{I}_s \\ \dot{U}_{CD} = jX_s\dot{I}_s + j\omega M\dot{I}_p \end{cases} \tag{2}$$

where X_p and X_s are the primary and secondary reactances. For n switching frequencies, they are, Eqn. (3) shown at the bottom of this page where

$$\begin{cases} \omega_{p1} = \frac{1}{\sqrt{L_{p1}C_{p1}}}, \omega_{p2} = \frac{1}{\sqrt{L_{p2}C_{p2}}}, \omega_{p3} = \frac{1}{\sqrt{L_{p2}C_{p3}}}, \dots \\ \dots, \omega_{p2(n-1)} = \frac{1}{\sqrt{L_{pn}C_{p2(n-1)}}}, \omega_{p(2n-1)} = \frac{1}{\sqrt{L_{pn}C_{p(2n-1)}}} \\ \omega_{s1} = \frac{1}{\sqrt{L_{s1}C_{s1}}}, \omega_{s2} = \frac{1}{\sqrt{L_{s2}C_{s2}}}, \omega_{s3} = \frac{1}{\sqrt{L_{s2}C_{s3}}}, \dots \\ \dots, \omega_{s2(n-1)} = \frac{1}{\sqrt{L_{sn}C_{s2(n-1)}}}, \omega_{s(2n-1)} = \frac{1}{\sqrt{L_{sn}C_{s(2n-1)}}} \end{cases}$$

and ω_i ($i = 1,2,\dots,n$) represents each switching frequency from 1 to n. X_{pi} and X_{si} ($i = 1,2,\dots,n$) are the primary and secondary reactances over n switching frequencies.

When the primary side is detuned and the secondary side is tuned, the output power is

$$P = \frac{U_{AB}^2 R_{\text{eq}}}{\left(\omega_i^2 L_p L_s\right) k^2 + \frac{\left(R_{\text{eq}} X_{pi}\right)^2}{\left(\omega_i^2 L_p L_s\right) k^2}} \quad (i = 1, 2, \dots, n). \tag{4}$$

Power versus coupling coefficient characteristics with a constant X_{pi} are shown in Fig. 3 for three switching frequencies, each corresponding to one of the resonant tanks. As shown in Fig. 3, the output power at each switching frequency has a maximum at an ideal value of k and decreases away from this value. These curves intersect at specific coupling coefficients. We can operate within a predetermined power variation range with a strategy that selects the appropriate switching frequency as a function of k. The useful misalignment range can be extended by using multiple switching frequencies.

With n switching frequencies ($f_1 < f_2 < \cdots < f_n$), define the coupling range for switching frequency 1, f_1, as $k_{\min 1} \le k \le k_{\max 1}$, the coupling range for switching frequency 2, f_2, as $k_{\min 2} \le k \le k_{\max 2}$, and so on. Consider a coupling range from $k_{\min i}$ to $k_{\max i}$ for each switching frequency f_i ($i = 1,2,\dots,n$). A power

$$\begin{cases} X_{pi} = L_{p1}\left(\omega_i - \frac{\omega_{p1}^2}{\omega_i}\right) + \frac{L_{p2}\left(\omega_i - \frac{\omega_{p2}^2}{\omega_i}\right)}{1+\frac{\omega_{p2}^2-\omega_i^2}{\omega_{p3}^2}} + \dots + \frac{L_{pn}\left(\omega_i - \frac{\omega_{p2(n-1)}^2}{\omega_i}\right)}{1+\frac{\omega_{p2(n-1)}^2-\omega_i^2}{\omega_{p(2n-1)}^2}} \\ X_{si} = L_{s1}\left(\omega_i - \frac{\omega_{s1}^2}{\omega_i}\right) + \frac{L_{s2}\left(\omega_i - \frac{\omega_{s2}^2}{\omega_i}\right)}{1+\frac{\omega_{s2}^2-\omega_i^2}{\omega_{s3}^2}} + \dots + \frac{L_{sn}\left(\omega_i - \frac{\omega_{s2(n-1)}^2}{\omega_i}\right)}{1+\frac{\omega_{s2(n-1)}^2-\omega_i^2}{\omega_{s(2n-1)}^2}} \end{cases} \quad (i = 1, 2, \dots, n) \tag{3}$$

variation coefficient Γ_{pi} can be defined as

$$\Gamma_{pi} = \frac{P_{\max i} - P_{\min i}}{P_{\text{rated}}} \tag{5}$$

where $P_{\min i}$ and $P_{\max i}$ are the minimum and maximum output power within that range. The design practice here is to set P_{rated} to the maximum in Fig. 3. This defines a nominal coupling coefficient for each switching frequency, and the derivative of (4) with respect to k should be zero at $k = k_{\text{nom}i}$

$$\frac{\partial P}{\partial k}\,|_{k=k_{\text{nom}i}} = 0\,(X_{pi} \neq 0)$$

$$\Rightarrow k_{\text{nom}i} = \sqrt{\frac{R_{\text{eq}} X_{pi}}{\omega_i^2 L_p L_s}} \quad (i = 1, 2, \ldots, n)\,. \tag{6}$$

Here, $k_{\text{nom}\,i}$ corresponds to maximum output power for each switching frequency. Combining (4) and (6), the maximum output power $P_{\max i}$ for each switching frequency is

$$P_{\text{rated}} = P_{\max i} = \frac{U_{AB}^2}{2X_{pi}} \quad (i = 1, 2, \ldots, n)\,. \tag{7}$$

This indicates $P_{\max i}$ (given high component Q) is affected only by the primary reactance X_{pi}. Once X_{pi} is determined, regardless of the values of R_o, the maximum output power can be determined. The system has consistent output power capability as the load changes, which is beneficial to reduce charging time in battery charging applications.

There are other possibilities for the power versus coupling coefficient curve: $k_{\min i} \leq k_{\max i} \leq k_{\text{nom}i}$, and $k_{\text{nom}i} \leq k_{\min i} \leq k_{\max i}$, but the power variation in these cases is higher. To minimize the power variation coefficient Γ_{pi}, curves with an intermediate peak as in Fig. 3 should be used and the minimum output power at the maximum and minimum coupling coefficients should match [28], so

$$P_{\min i} = P\,(k_{\max i}) = P\,(k_{\min i})\,. \tag{8}$$

The corresponding primary reactance can be obtained by solving (6) and (8), and is

$$\begin{cases} X_{pi} = \frac{\alpha_i \omega_i^2 L_p L_s k_{\min i}^2}{R_{\text{eq}}} \\ k_{\max i} = \alpha_i k_{\min i} (\alpha_i > 1) \end{cases} \quad (i = 1, 2, \ldots, n) \tag{9}$$

where α_i (i = 1,2,…, n) is a coupling variation ratio over n switching frequencies.

Substituting (7)–(9) into (5), the power variation coefficient Γ_{pi} becomes

$$\Gamma_{pi} = \frac{(\alpha_i - 1)^2}{\alpha_i^2 + 1}\,(i = 1, 2, \ldots, n)\,. \tag{10}$$

This shows that the power variation coefficient is affected only by the target coupling variation ratio. Once the coupling coefficient range is determined, the power variation will follow from (10) and vice versa. One implication of (10) is that narrow power variation is linked to narrow coupling variation. For one frequency, power variation below 10% requires $\alpha < 1.6$. The number of switching frequency choices n supports a coupling range of $\alpha_1 \times \alpha_2 \times \cdots \times \alpha_n$. For 10% variation, two switching frequencies support about a 2.5:1 coupling range, three would support about a 4:1 range, and so on. This suggests that two or three frequencies will give useful results in practical systems and that more frequencies could expand the coupling range substantially. For example, it is possible to support a 10:1 coupling range with power variation below 15% by choosing $\alpha = 1.79$ and $n = 4$.

The input impedance angle θ from $k_{\min i}$ to $k_{\max i}$ can be obtained from (2) and (9) as

$$\theta = \arctan\left(\frac{X_{pi} R_{\text{eq}}}{\omega_i^2 M^2}\right) \Rightarrow \arctan\left(\frac{\alpha_i k_{\min i}^2}{k^2}\right). \tag{11}$$

This indicates that the input impedance angle variation is also affected only by the coupling variation ratio. For a given α, the input impedance angle variation is from arctan(1/α) to arctan(α). Circuit analysis shows that system active power is proportional to primary current and cos(θ) with a constant input first-harmonic voltage. The primary current will be affected only by the input impedance angle for constant system power. This means the primary current range is also consistent for a given α.

For a practical system, it is useful to constrain the power variation to match across the selected coupling ranges. In the case of n frequencies, this implies that the maximum and minimum output power for those selected switching frequencies should be equal, as suggested in Fig. 3. When k is in the lower coupling range, a higher switching frequency is used, and a lower switching frequency is used in the higher coupling range. The design targets are

$$\begin{cases} P_{\max 1} = P_{\max 2} = \cdots = P_{\max(n)} = P_{rated} \\ k_{\max 2} = k_{\min 1}, k_{\max 3} = k_{\min 2}, \ldots, k_{\max(n)} = k_{\min(n-1)} \\ \Gamma_{p1} = \Gamma_{p2} = \cdots = \Gamma_{p(n)}. \end{cases} \tag{12}$$

Combining (4), (7), (9), (10), and (12), the results imply

$$\begin{cases} X_p = X_{p1} = X_{p2} = \cdots = X_{p(n)} = \frac{U_{AB}^2}{2P_{\text{rated}}} \\ X_s = X_{s1} = X_{s2} = \cdots = X_{s(n)} = 0 \\ \alpha_1 = \alpha_2 = \cdots = \alpha_n = \alpha > 1 \\ \alpha^n k_{\min(n)} = \alpha^{n-1} k_{\max(n)} = \cdots = \alpha k_{\max 2} \\ \qquad = \alpha k_{\min 1} = k_{\max 1} \\ \alpha^{n-1}\omega_1 = \alpha^{n-2}\omega_2 = \cdots = \omega_n \\ M_{\max 1}^2 = k_{\max 1}^2 L_p L_s = \frac{\alpha_1 R_{\text{eq}} X_p}{\omega_1^2}. \end{cases} \tag{13}$$

From (13), these discrete frequencies are affected only by the choice of coupling variation ratio α. Once one switching frequency is predetermined, regardless of the values of R_{o} and P_{rated}, the other switching frequencies can be obtained based on consistent power variation. The initial predetermined frequency will be constrained by power device limitations and inductor volume.

III. Output Characteristics and Misalignment Performance Comparisons

A. Output Characteristics of the Proposed Topology

As mentioned in Section II, given values of n, Γ_p, $k_{\max 1}$, L_p, ω_1, R_{o}, and rated output power, system performance can be determined for a target misalignment range.

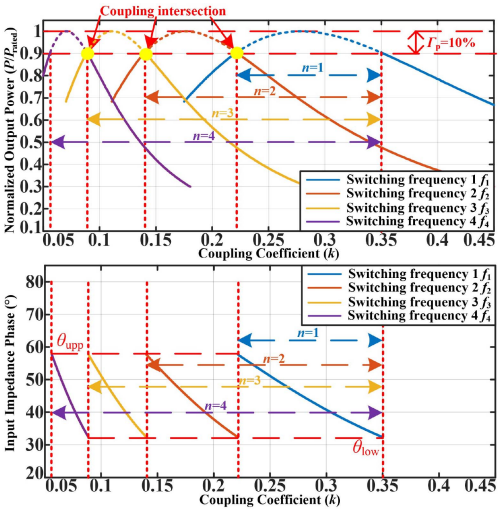

Fig. 4. Normalized output power and input impedance angle versus the coupling coefficient for $\alpha = 1.58$, $k_{\max} = 0.35$, $\Gamma_p = 10\%$, $n = 1$–4.

1) Output Characteristics of the Proposed Topology for Different Numbers of Switching Frequencies:

a) Output characteristics: As an example, normalized output power and input impedance angle versus coupling coefficient for $\alpha = 1.58$, $k_{\max} = 0.35$, and $\Gamma_p = 10\%$ are shown in Fig. 4 for up to four switching frequencies. The output power has been normalized to the rated (maximum) power P_{rated}.

As shown in Fig. 4, the power versus coupling coefficient curves at different switching frequencies intersect. Based on the specified Γ_p value, the top parts of the curves shown in dashed lines are the intended range of operating conditions and reflect different ranges of coupling. The overall range of k increases with the number of switching frequencies as α^n. The controller should change the switching frequency at the coupling intersection points highlighted in Fig. 4. In this example, f_1 corresponds to a coupling coefficient range from 0.22 to 0.35, f_2 corresponds to a coupling coefficient range from 0.14 to 0.22, f_3 corresponds to a coupling coefficient range from 0.088 to 0.14, and so on.

The input impedance is inductive over the entire coupling coefficient range. This supports ZVS switching control over the operating range. As shown in Fig. 4, the input impedance angle has the same upper and lower limits, θ_{upp} and θ_{low} for each frequency. This means that the range of primary current magnitudes will be the same for each selected switching frequency. This limited current range implies a limited reactive power range. Thus, the coupling range (and misalignment range) can be extended without requiring excessive reactive power or primary current. The limited reactive power range and ZVS operation enhance efficiency compared to conventional single-frequency compensation.

b) Control approach: A strategy must be provided to choose the appropriate switching frequency during operation. It can be implemented by measuring the input impedance angle between the first-harmonic input voltage and primary current to judge how to select the switching frequency, since the input impedance angle range gives consistent results for each switching frequency, as shown in Fig. 4. The control structure is shown in Fig. 5 and a flowchart of the strategy is shown in Fig. 6. The initial switching frequency is set to the highest allowed value, which starts the system at a low power level and input impedance angle.

The controller uses a DSP and does not require communication between the primary and secondary sides. It comprises impedance angle detection, frequency selection, and gate signal generation. The strategy sets upper and lower limits on the input impedance angle, θ_{upp} and θ_{low}. Based on the expected input impedance angle and accuracy of the input impedance angle detection, hysteresis should be added to the control to avoid chatter in the selection of frequency across intersection points. When the measured impedance angle is higher than the upper limit θ_{upp}, the frequency will switch to the next higher adjacent frequency. When the measured impedance angle is lower than the lower limit θ_{low}, the frequency will switch to the next lower adjacent frequency. In this system, the control can be set to operate only within the limits—meaning there are limits on the allowed coupling coefficient range (and misalignment range). The system can be allowed to operate somewhat beyond these angle limits if even more misalignment tolerance is desired, but the angle limits can be enforced to set design and operation limits.

2) Output Characteristics of the Proposed Topology Over a Load Range: Normalized output power for three load resistances is shown in Fig. 7 for up to four switching frequencies. From (7), the maximum output power is independent of load. As load (or equivalent battery impedance) changes, output power can be held almost constant, which is beneficial to determine charging time. Conventional modulation can be employed to adjust the output voltage or control the output power, as in (7), and this process is also independent of load.

As shown in Fig. 7, for a given coupling variation ratio α, the maximum output power and power variation range are determined. When the load changes, the corresponding coupling coefficient for a given power variation range will change. For example, while enforcing a 10% power variation limit with $n = 2$, a 40 Ω load can be supported over a coupling range from 0.11 to 0.29, a 60 Ω load can be supported over a coupling range from 0.14 to 0.35, and an 80 Ω load can be supported over a coupling range from 0.16 to 0.4. To hold the variation limit on a worst case basis, the combined coupling coefficient range is from 0.16 to 0.29 over a 2:1 load range. The change with respect to load must be considered to provide margin and be sure the overall target power variation range can be supported over the allowed load values.

B. Comparisons to Conventional Frequency Controls

In conventional single-frequency S-S compensation, there are two typical frequency control methods for misalignment conditions that include tracking unity power factor [26] and maintaining consistent output power [30]. In the following, the proposed method takes two-frequency compensation as an example to compare to these two conventional methods.

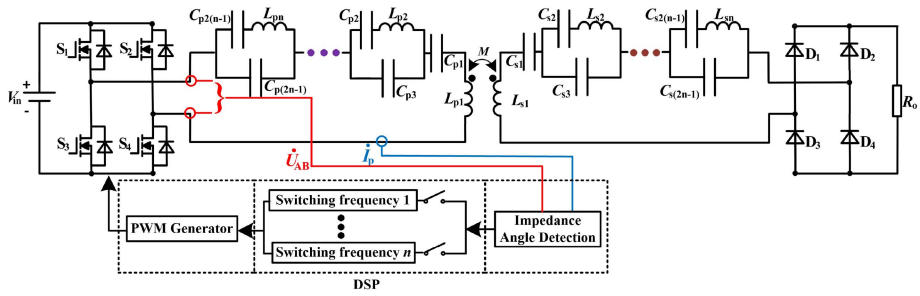

Fig. 5. Closed-loop control structure of the proposed method.

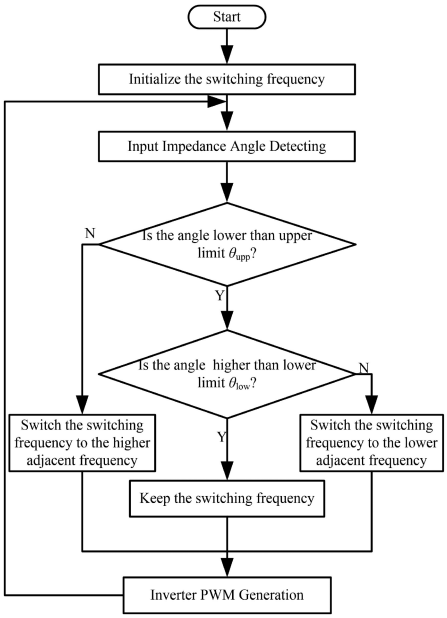

Fig. 6. Flowchart for the control approach with the proposed method.

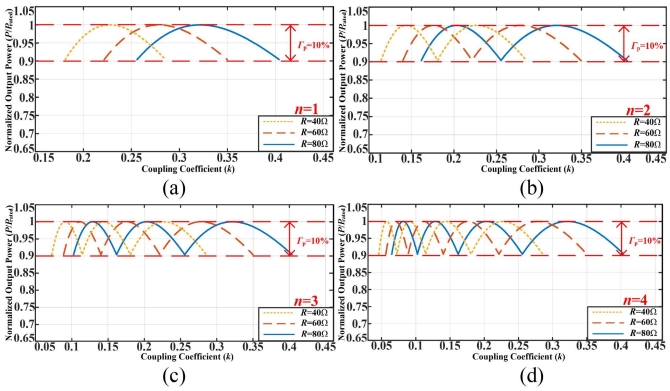

Fig. 7. Normalized output power for three load resistances with: (a) one switching frequency, (b) two switching frequencies, (c) three switching frequencies, and (d) four switching frequencies.

1) Comparisons to Frequency Control for Unity Power Factor (Referred to Here as Frequency Control Method 1): When the switching frequency matches primary and secondary resonances, the system can achieve input unity power factor. The output power $P_{\text{S-S\_UPF}}$ will be

$$P_{\text{S-S\_UPF}} = \frac{U_{AB}^2 R_{\text{eq}}}{(\omega^2 L_p L_s)\, k^2}. \tag{14}$$

This is proportional to $1/k^2$ for a given load. In Fig. 8, this conventional single-frequency control is compared to the proposed two-frequency power variability control. Over the 2.5:1 coupling range explored in the figure, the output power with frequency control method 1 varies by a factor of 6.25:1. The associated resonant currents also show a 6.25:1 range and the maximum primary capacitor voltage will be about 14.3 times the input voltage. If this method is modified to combine PWM controls and limit power variation [33], the primary current still covers a 2.5:1 range and the maximum primary capacitor voltage is about 5.7 times the input voltage. In contrast, the proposed two-frequency control exhibits output power variation of only 10% and a current range of 1.56:1 for 2.5:1 coupling variation.

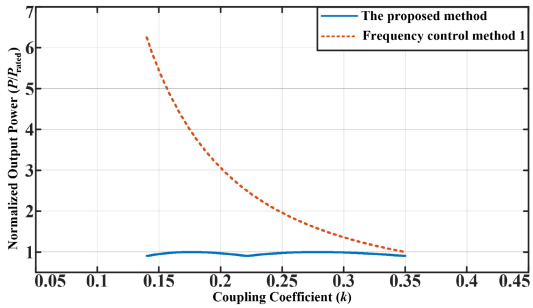

Fig. 8. Comparisons between normalized IPT system output power with the proposed method and with frequency control method 1 when the coupling coefficient ranges from 0.14 to 0.35.

2) Comparisons to Frequency Control for Consistent Output Power (Referred to Here as Frequency Control Method 2): An alternative conventional control could select a variable switching frequency to enforce consistent output power. In this case, the switching frequency is adjusted away from resonance to maintain fixed output power. The primary and secondary sides will detune, and the input impedance angle will be

$$\theta = \arctan\left(\frac{X_p R_{\text{eq}}^2 - \left(\omega^2 M^2 - X_p X_s\right)\cdot X_s}{\omega^2 M^2 R_{\text{eq}}}\right). \tag{15}$$

Based on this angle, when the mutual inductance (and the coupling coefficient) decreases, the input impedance angle will

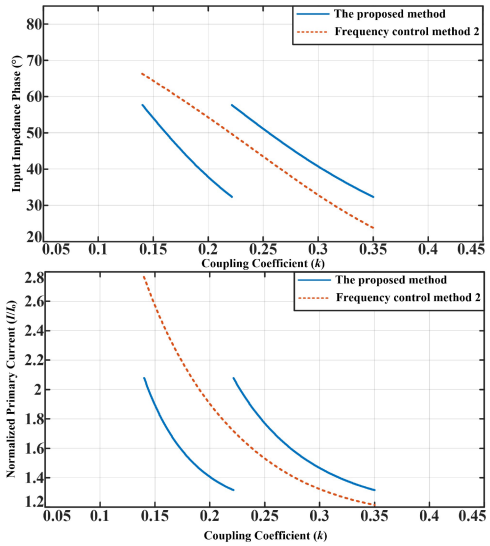

Fig. 9. Comparisons between normalized IPT system primary current with the proposed method and with frequency control method 2 over a coupling coefficient range from 0.14 to 0.35.

increase. Impedance angle and primary current for this control are compared to the proposed two-frequency approach in Fig. 9. The proposed method acts in sections as the frequency changes. The conventional approach shows a much wider variation of impedance angle and primary current over a coupling range from 0.14 to 0.35. The maximum primary current with the proposed method is at least 25% lower than with frequency control method 2. The maximum voltage across the capacitor with frequency control method 2 is about 8.9 times the input voltage.

IV. Design Procedures

In this section, a design procedure for multifrequency compensation is presented. The number of switching frequencies can be selected by trading off misalignment range, power variation, and power loss in additional resonant tanks. The parameters can be determined by selecting current ratios. A flowchart of the design procedure is given in Fig. 10.

A. Limits on the Number of Switching Frequencies

The analysis so far is based on ideal conditions, but equivalent series resistances (ESRs) and component tolerances will affect system performance. Each added switching frequency requires an additional resonant tank. Component ESRs will degrade system performance and reduce efficiency. Component tolerances will affect resonant performance. In this section, practical limits on performance and switching frequency count are discussed.

1) Effect of Component Series Resistances:

a) Resonant performance: Reactances of a multifrequency resonant tank will differ from the ideal, given ESR. Reactances of the multifrequency resonant network, considering ESR versus frequency, are shown in Fig. 11, where f_{r1} is the first resonant frequency, f_{r2} is the second resonant frequency, and so on. These examples use $\alpha = 1.58$, $k_{\max} = 0.35$, $\Gamma_p = 10\%$,

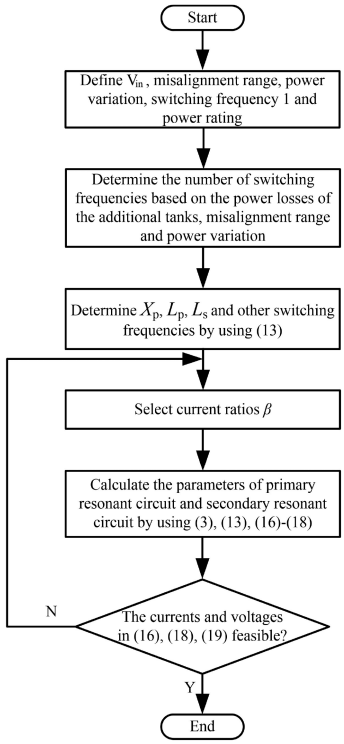

Fig. 10. Flowchart for design with the proposed method.

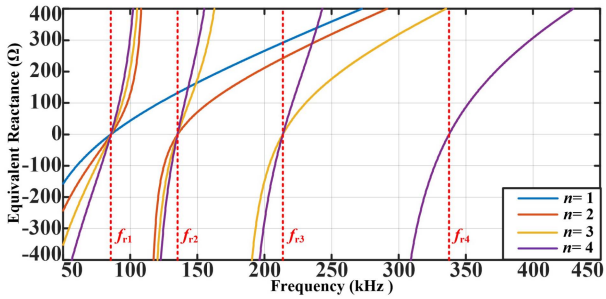

Fig. 11. Reactances of the multifrequency resonant network considering series resistances versus the frequency for different numbers of switching frequencies.

$Q_{\text{coil}} = 600$, and $Q_L = 800$, where Q_{coil} is the quality factor of the coil and Q_L is the quality factor of each added inductor.

As shown in Fig. 11, over the range $n = 1$ to 4, the resonant frequency of the multifrequency resonant network changes little, and the frequency tolerance decreases as Q_L increases. This means that although additional resonant tanks introduce more ESR, they have little impact on resonant performance when Q_L is high.

b) Output performance: ESRs lead to extra losses and affect output power. Normalized output power considering ESR versus coupling coefficient for different numbers of switching frequencies is shown in Fig. 12. When n increases from 1 to 4, the output power in a given coupling coefficient range decreases because of ESR. Losses will increase with the number of switching frequencies and extra output power margin will be needed at low coupling to compensate. In Fig. 12, for example, the original target of 10% power variation expands to about 15%

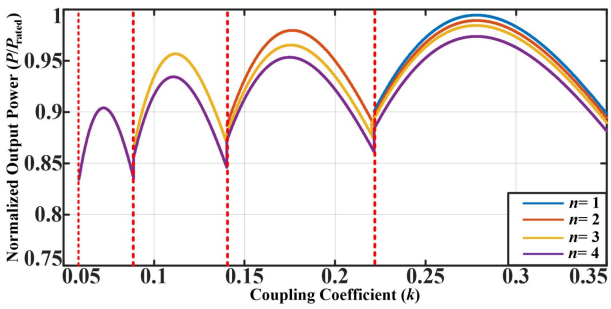

Fig. 12. Normalized output power considering series resistances versus the coupling coefficient for different numbers of switching frequencies.

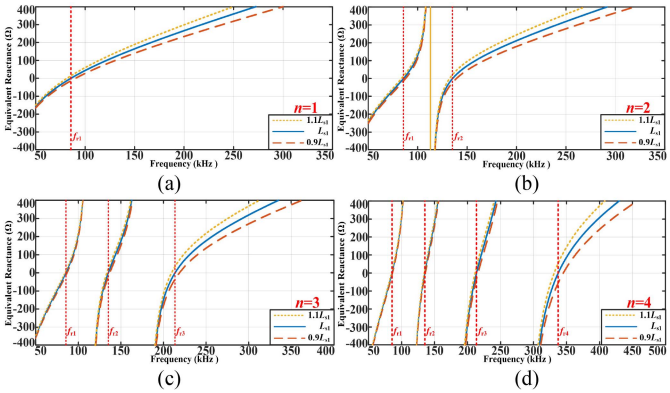

Fig. 13. Reactances of the secondary resonant network considering component tolerance of L_{s1} for different numbers of switching frequencies at $\alpha = 1.58$, $k_{\max} = 0.35$: (a) $n = 1$, (b) $n = 2$, (c) $n = 3$, and (d) $n = 4$.

as n increases to four, and maximum power drops by almost 10% at low coupling. The practical implication is that $n = 4$ is probably an upper limit for a useful design.

2) Effect of Component Tolerances: Component tolerances will affect resonance. Fig. 13 shows effects of ±10% component tolerance in L_{s1} based on (3). The plots show reactance versus frequency for different numbers of switching frequencies at $\alpha = 1.58$ and $k_{\max} = 0.35$. When L_{s1} varies over this range, resonant frequencies will change. The lower the frequency, the lower the deviation from the ideal value. The maximum resonant frequency variation occurs at the highest switching frequency and decreases with more switching frequencies. Frequency tolerance will decrease as the number of switching frequencies increases. For best performance, each switching frequency needs a fine-tuned adjustment to maintain the desired output characteristic.

3) Selection of the Number of Switching Frequencies: Selection of the number of switching frequencies is based on a tradeoff between the target misalignment range, power variation, power losses of additional resonant tanks, and component tolerance effects. Fig. 12 motivates a limit $n \leq 4$ based on power loss. In previous single-frequency compensation [25], [26], the coupling coefficient range is about 2:1 and the power variation is about 20%. In this article, based on comprehensive consideration of power losses of the added resonant tanks, misalignment range, and power variation, a two-frequency compensation circuit has been designed over a 2.5:1 coupling coefficient range (the target coupling range in this article is from 0.14 to 0.35) and 10% power variation. Fig. 12 suggests that $n = 3$ would reduce output power at low coupling by about 3% and could be feasible if the extra loss can be accepted.

B. Parameter Design for the Proposed Topology

This section takes two-frequency compensation as an example to present parameter selection based on inductor currents and capacitor voltages. The currents through L_{p2} and L_{s2} at the selected switching frequencies are

$$\begin{cases} I_{L_{p2}1} = \dfrac{I_p}{\left|1-\omega_1^2 L_{p2}C_{p3}+\frac{C_{p3}}{C_{p2}}\right|}, I_{L_{p2}2} = \dfrac{I_p}{\left|1-\omega_2^2 L_{p2}C_{p3}+\frac{C_{p3}}{C_{p2}}\right|} \\ I_{L_{s2}1} = \dfrac{I_s}{\left|1-\omega_1^2 L_{s2}C_{s3}+\frac{C_{s3}}{C_{s2}}\right|}, I_{L_{s2}2} = \dfrac{I_s}{\left|1-\omega_2^2 L_{s2}C_{s3}+\frac{C_{s3}}{C_{s2}}\right|} \end{cases} \tag{16}$$

where I_{Lp21} and I_{Lp22} are currents through L_{p2} at ω_1 and ω_2 and I_{Ls21} and I_{Ls22} are currents through L_{s2} at ω_1 and ω_2. To minimize the maximum inductor current, I_{Lp21} (I_{Ls21}) should match I_{Lp22} (I_{Ls22}), so (16) becomes

$$\begin{cases} I_{L_{p2}1} = I_{L_{p2}2} = \beta_1 I_p \\ I_{L_{s2}1} = I_{L_{s2}2} = \beta_2 I_s \end{cases} \tag{17}$$

where β_1 and β_2 are ratios of the primary and secondary resonant currents. It follows that the voltages across capacitors C_{p2} and C_{p3} are

$$\begin{cases} U_{C_{p2}1} = \frac{I_{L_{p2}1}}{\omega_1 C_{p2}} = \frac{\beta_1 I_p}{\omega_1 C_{p2}}, U_{C_{p2}2} = \frac{I_{L_{p2}2}}{\omega_2 C_{p2}} = \frac{\beta_1 I_p}{\omega_2 C_{p2}} \\ U_{C_{p3}1} = \left(\omega_1 L_{p2} - \frac{1}{\omega_1 C_{p2}}\right)\beta_1 I_p, \\ U_{C_{p3}2} = \left(\omega_2 L_{p2} - \frac{1}{\omega_2 C_{p2}}\right)\beta_1 I_p \end{cases} \tag{18}$$

where U_{Cp21} and U_{Cp22} are voltages across C_{p2} at ω_1 and ω_2 and U_{Cp31} and U_{Cp32} are voltages across C_{p3} at ω_1 and ω_2. Analogous to the primary resonant circuit, voltages across secondary capacitors C_{s2} and C_{s3} are

$$\begin{cases} U_{C_{s2}1} = \frac{I_{L_{s2}1}}{\omega_1 C_{s2}} = \frac{\beta_2 I_s}{\omega_1 C_{s2}}, U_{C_{s2}2} = \frac{I_{L_{s2}2}}{\omega_2 C_{s2}} = \frac{\beta_2 I_s}{\omega_2 C_{s2}} \\ U_{C_{s3}1} = \left(\omega_1 L_{s2} - \frac{1}{\omega_1 C_{s2}}\right)\beta_2 I_s, \\ U_{C_{s3}2} = \left(\omega_2 L_{s2} - \frac{1}{\omega_2 C_{s2}}\right)\beta_2 I_s \end{cases} \tag{19}$$

where U_{Cs21} and U_{Cs22} are C_{s2} voltages and U_{Cs31} and U_{Cs32} are C_{s3} voltages.

Take the primary circuit as an example. From (16)–(18), voltages across C_{p2} and C_{p3} versus primary current ratio β_1 are shown in Fig. 14, where capacitor voltages have been normalized to the input voltage V_{in} (this example uses 300 V). Fig. 14 shows that higher current ratios reduce voltage rating requirements for these four capacitors. A good choice of β_1 is in the range 1.1 to 1.5. In this example, this ratio range keeps inductor currents and capacitor voltages below about 3 per unit, which is much lower than the previous method in Section III-B. This means that the proposed method offers benefits in high-power IPT systems compared to prior work. The same range applies to β_2. After selecting the current ratios of different inductors, multifrequency circuit parameters can be determined from (3), (13), and (16)–(19).

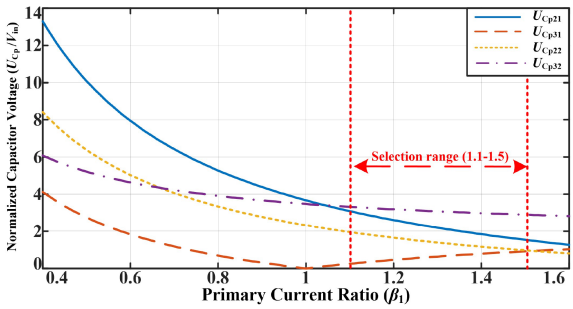

Fig. 14. Voltages across C_{p2} and C_{p3} versus primary current ratio at $V_{\text{in}} = 300$ V.

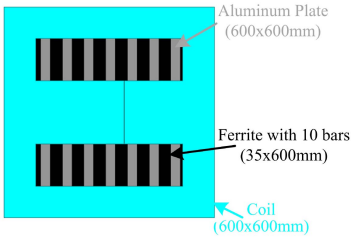

Fig. 15. DD structure for the proposed IPT system.

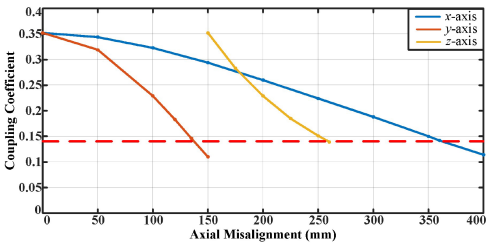

Fig. 16. Coupling coefficient characteristics versus axial misalignment, from simulation results.

C. Design of the Loosely Coupled Transformer

The loosely coupled transformer transfers power through a large air gap and seeks to maximize coupling coefficient and quality factor. A double-D coupler has been used here to build the IPT system because of its high flux path geometry [18]. ANSYS MAXWELL was used to assist in the design. The geometry and specifications of the DD structure design are shown in Fig. 15 and were used to implement the experiments.

Coupling coefficients with x-axis, y-axis, and z-axis misalignment are shown in Fig. 16 for single-axis misalignment based on nominal offsets $x = 0$, $y = 0$, and $z = 150$ mm. The target coupling coefficient range of 0.14 to 0.35 corresponds to maximum misalignment values in x-axis and y-axis directions of about 360 and 135 mm, respectively. The range corresponds to z-axis (air gap) distances between 150 and 260 mm. The x-axis direction has the widest range and the z-axis direction has the narrowest range because the magnetic field of the double-D structure is polar and directional [18].

From (10), the power variation range depends only on the coupling coefficient range. This means that other coupled structures can be used, although they will correspond to different misalignment ranges. It also means that multiaxis misalignment is cumulative in a simple manner. In Fig. 16, for example, a y-axis misalignment of 50 mm will reduce k from 0.35 to about 0.32. This becomes a starting point for x-axis misalignment, and so on.

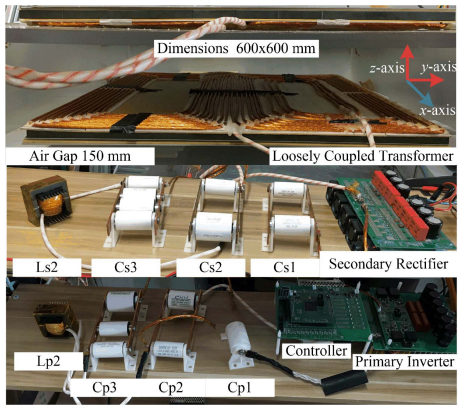

Fig. 17. Experimental platform for the proposed topology.

TABLE I
SPECIFICATIONS OF THE TWO-FREQUENCY TOPOLOGY

Parameters	Symbols	Measured Values
Primary inductances	L_{p1}, L_{p2}	203.7 μH, 128.9 μH
Secondary inductances	L_{s1}, L_{s2}	259.3 μH, 149.0 μH
Primary capacitor	C_{p1}, C_{p2}, C_{p3}	19.3 nF, 31.4 nF, 29.8 nF
Secondary capacitor	C_{s1}, C_{s2}, C_{s3}	11.2 nF, 30.7 nF, 23.5 nF
Switching frequency	f_1 , f_2	85.5 kHz, 135.1 kHz
Power rating	P_{rated}	1.5 kW
Input voltage	V_{in}	300 V
Load resistance	R_o	60 Ω
Allowed coupling range	k	0.14–0.35
Power variation coefficient	Γ_p	10%

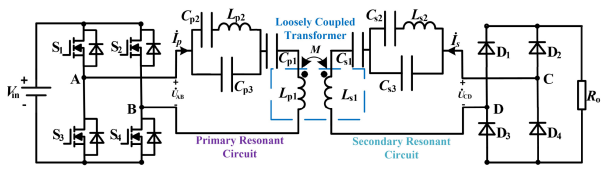

Fig. 18. Two-frequency compensation topology for the proposed method.

V. Experimental Results

A. Experimental Results

1) Experimental Results for Two-Frequency Compensation: The 1.5 kW prototype IPT system shown in Fig. 17 was prepared to test two-frequency and three-frequency operations. Specifications and parameters for two-frequency operation are given in Table I. The two-frequency compensation topology is shown in Fig. 18. Fig. 19 shows how primary and secondary inductances change over the target coupling coefficient range. The values change only about 1%, so they can be treated as constant during operation. An SiC MOSFET module (SK25MH120TSCp) forms the full-bridge inverter and four ultrafast soft

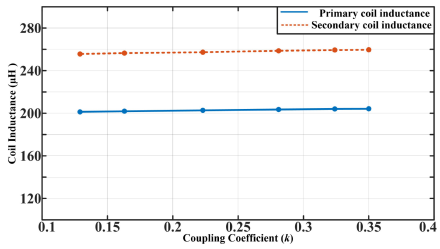

Fig. 19. Coil inductances versus coupling coefficient for experimental system.

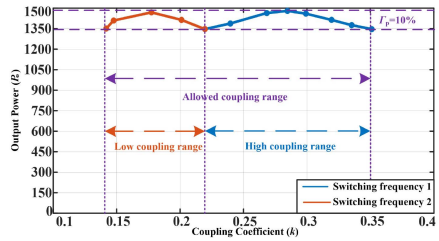

Fig. 20. Experimental results of output power for two-frequency compensation within the allowed coupling range at $R_o = 60\ \Omega$.

recovery diodes (VS-C4PU6006LHN3) form the rectifier bridge. A TMS320F28335 processor generates switching signals. Film capacitors are used in the resonant tanks and resonant inductors are designed based on [35]. Load resistances are used at the output. Based on specifications in Table I, when the coupling coefficient is between 0.22 and 0.35, switching frequency $f_1 = 85.5$ kHz is used. When the coupling coefficient is between 0.14 and 0.22, switching frequency $f_2 = 135.1$ kHz is used.

Fig. 20 shows output power with two-frequency compensation over a coupling range from 0.14 to 0.35. The measured output power variation was 1348 to 1470 W in the low coupling range and 1347 to 1481 W in the high coupling range. The ouput characteristics are consistent at these two switching frequencies, and the power variation coefficient is below 10% over the entire allowed coupling coefficient range. From (10), notice that a single frequency over this 2.5:1 coupling range would have given power variation of at least 30% instead.

Fig. 21(a)–(d) show experimental voltage and current waveforms for two-frequency compensation at switching frequencies of 135.1 and 85.5 kHz for various coupling coefficients. Fig. 21(a) and (b) show results at 135.1 kHz, when the coupling coefficient is 0.14 and 0.22, respectively. Fig. 21(c) and (d) illustrate results at 85.5 kHz, with coupling coefficients of 0.22 and 0.35, respectively. The system can maintain ZVS over the allowed coupling range. At the coupling intersection, primary current is lower for the higher switching frequency.

2) Experimental Results for Three-Frequency Compensation: An additional resonant tank was added to test three-frequency compensation over the target coupling coefficient range (0.14-0.35). Parameters for three-frequency operation are given in Table II. The three-frequency compensation topology is shown in Fig. 22. It should be mentioned that the current ratio of L_{p2} (L_{s2}) is matched at switching frequencies 1 and 2, and the

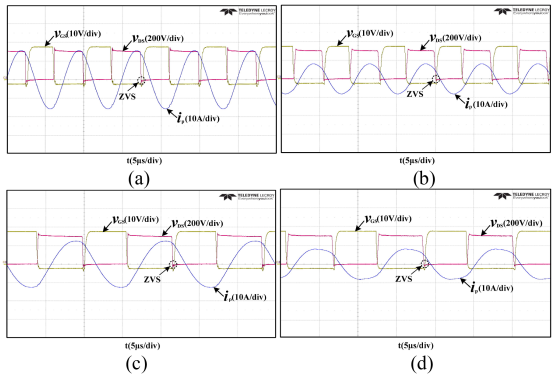

Fig. 21. Experimental waveforms for $n = 2$ at $R_o = 60\ \Omega$ and different coupling coefficients: (a) 135.1 kHz at $k = 0.14$, (b) 135.1 kHz at $k = 0.22$, (c) 85.5 kHz at $k = 0.22$, and (d) 85.5 kHz at $k = 0.35$.

TABLE II
SPECIFICATIONS OF THE THREE-FREQUENCY TOPOLOGY

Parameters	Symbols	Measured Values
Primary inductances	L_{p1}, L_{p2}, L_{p3}	188.6 μH, 119.7 μH, 143.9 μH
Secondary inductances	L_{s1}, L_{s2}, L_{s3}	240 μH, 138.5 μH, 169.1 μH
Primary capacitor	C_{p1}, C_{p2}, C_{p31}, C_{p4}, C_{p5}	25.7 nF, 18.9 nF, 26.3 nF, 29 nF, 40.4 nF
Secondary capacitor	C_{s1}, C_{s2}, C_{s3}, C_{s4}, C_{s5}	13.6 nF, 17.5 nF, 20.8 nF, 26.4 nF, 31.5 nF
Switching frequency	f_1, f_2, f_2	85.5 kHz, 115.1 kHz, 155.2 kHz
Power variation coefficient	Γ_p	5%

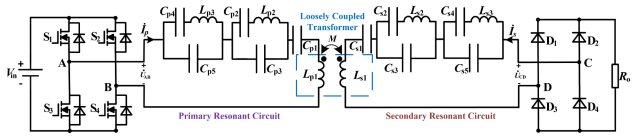

Fig. 22. Three-frequency compensation topology for the proposed method.

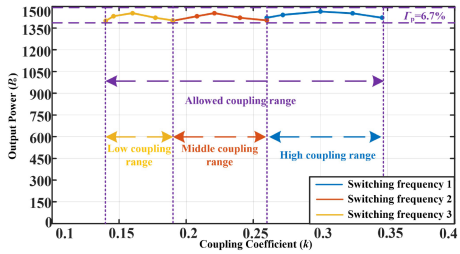

Fig. 23. Experimental results of output power for three-frequency compensation within the allowed coupling range at $R_o = 60\ \Omega$.

current ratio of L_{p3} (L_{s3}) is matched at switching frequencies 2 and 3. When the coupling coefficient is between 0.26 and 0.35 (high coupling range), $f_1 = 85.5$ kHz is selected. For $0.19 < k < 0.26$ (middle coupling range), $f_2 = 115.2$ kHz is selected. For $0.14 < k < 0.19$ (low coupling range), $f_3 = 155.2$ kHz is selected.

Fig. 23 shows output power with three-frequency compensation over a coupling range from 0.14 to 0.35. Output power

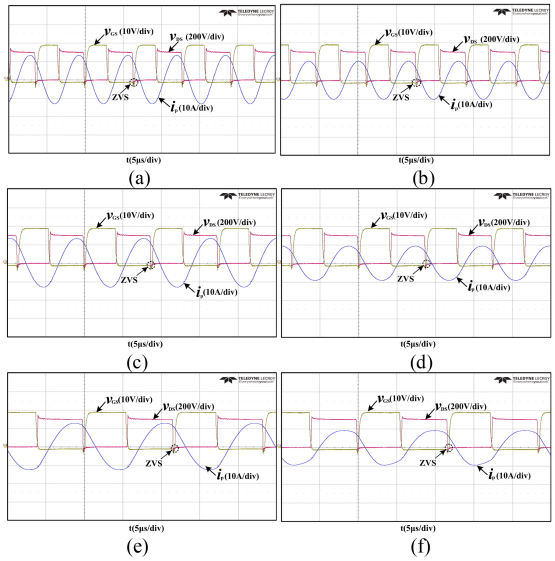

Fig. 24. Experimental waveforms for $n = 3$ at $R_o = 60\ \Omega$ and different coupling coefficients: (a) 155.2 kHz at $k = 0.14$, (b) 155.2 kHz at $k = 0.19$, (c) 115.1 kHz at $k = 0.19$, (d) 115.1 kHz at $k = 0.26$, (e) 85.5 kHz at $k = 0.26$, and (f) 85.5 kHz at $k = 0.35$.

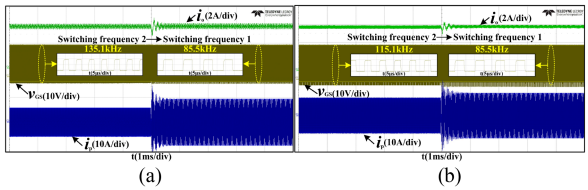

Fig. 25. Experimental transient waveforms for two-frequency and three-frequency compensations with $R_o = 60\ \Omega$ across a coupling intersection point. (a) Two-frequency compensation at $k = 0.22$. (b) Three-frequency compensation at $k = 0.26$.

variation was 1401 to 1453 W at low coupling, 1402 to 1454 W at middle coupling, and 1421 to 1465 W at high coupling. The power in low and middle coupling ranges is slightly lower as ESRs increase with frequency. Over the target coupling range, the maximum power variation is about 6.7%.

Fig. 24(a)–(f) show experimental waveforms for $n = 3$ with various coupling coefficients. Fig. 24(a) and (b) show results at 155.2 kHz, with $k = 0.14$ and 0.19, respectively. Fig. 24(c) and (d) illustrate results at 115.1 kHz, with $k = 0.19$ and 0.26, respectively. Fig. 24(e) and (f) show results at 85.5 kHz, with $k = 0.26$ and 0.35, respectively. The system can maintain ZVS over the allowed coupling range. At the coupling intersection, the primary current of each higher frequency is lower than that of each lower frequency. This will limit the primary current range and supports lower device power ratings. The maximum primary current with three frequencies is 14% less than with two-frequency compensation.

3) Transient Process: Fig. 25(a) and (b) show transient waveforms for two-frequency and three-frequency compensations at the coupling intersection point. The switching frequency changes at the coupling intersection. The transient process is completed within 0.35 ms for two-frequency compensation, and within 0.5 ms for three-frequency compensation. The primary

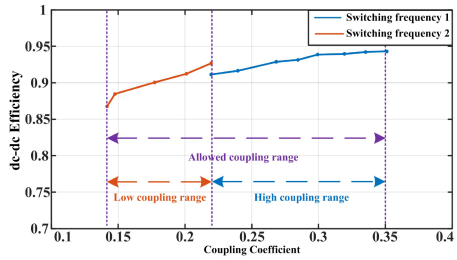

Fig. 26. DC–DC efficiency for two-frequency compensation within the allowed coupling range at $R_o = 60\ \Omega$.

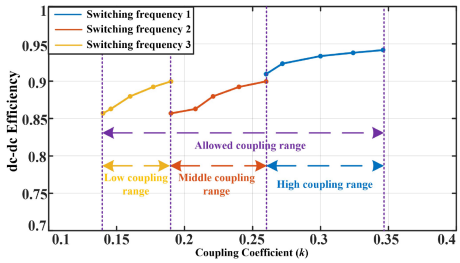

Fig. 27. DC–DC efficiency for three-frequency compensation within the allowed coupling range at $R_o = 60\ \Omega$.

current increases when each switching frequency drops because the input impedance angle and reactive power increase. Experimental results verify the expected system performance with the proposed method.

4) DC–DC Efficiency:

a) Two-frequency compensation: Fig. 26 shows dc–dc efficiency for two-frequency compensation. Efficiency decreases as coupling coefficient decreases. Efficiency in the low coupling range varies from 86.8% to 92.7%, and the minimum and maximum efficiency in the high coupling range are 91.1% and 94.6%. When $k = 0.22$ (at the coupling intersection), efficiency at the higher switching frequency is higher because of the lower reactive power and primary current. Efficiency in the high coupling range is higher because the ESRs of primary and secondary resonant circuits increase as the switching frequency increases.

b) Three-frequency compensation: Fig. 27 shows dc–dc efficiency for three-frequency compensation. Efficiency decreases as coupling coefficient decreases for each switching frequency. Efficiency ranges from 85.7% to 89.9% at low coupling, from 86.4% to 90.5% at middle coupling, and from 90.9% to 94.1% at high coupling. As shown in Fig. 27, when $k = 0.26$ (at the coupling intersection), because of the higher inductor currents and increased ESRs, efficiency at switching frequency 2 is a little lower than that at switching frequency 1. Efficiency at switching frequency 3 is only slightly lower than that at switching frequency 2. The maximum and minimum efficiencies of three-frequency compensation are 0.5% and 1.1% lower than those of two-frequency compensation.

Based on [37], loss analysis for two-frequency and three-frequency compensations at $k = 0.35$ is shown in Fig. 28. Power loss increases as the number of switching frequencies increases. For two-frequency operation, the extra inductors

TABLE III
COMPARISON TO RELATED RECENT WORK

Topology	[31]	[27]	[29]	[28]	Proposed topology
Numbers of coils	2	2	4	2	2
Numbers of added switches	0	0	0	2	0
Numbers of inductors	0	2	1	1	2
Numbers of capacitors	2	3	5	3	6
Total component number	4	7	10	8	10
Misalignment directions	*x*-, *y*-, and *z*-axis	*x*-, *y*-, and *z*-axis	*x*- and *z*-axis	*x*-, *y*-, and *z*-axis	*x*-, *y*-, and *z*-axis
Coupling variation ratio	180% (0.10–0.18)	200% (0.14–0.28)	233% (0.15–0.35)	250% (0.10–0.25)	250% (0.14–0.35)
Power fluctuation coefficient	Constant output	20%	10%	10%	10%
Rated Power	1000 W	100 W	3300 W	400 W	1500 W
Efficiency	75%–87%	83.5%–87.5%	85%–94%	85.5%–91.7%	86.8%–94.6%

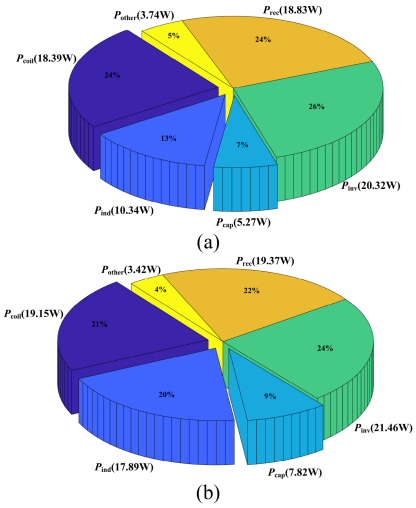

Fig. 28. Loss analysis for two-frequency and three-frequency compensations at $k = 0.35$. (a) Loss breakdown for two-frequency compensation. (b) Loss breakdown for three-frequency compensation.

reduce efficiency by about 0.7%, whereas this value is 1.2% in the three-frequency system.

With more switching frequencies, the power variation, maximum primary current, and reactive power will decrease over the target coupling range, compared to conventional controls. The efficiency will be slightly lower because of additional resonant tanks. In practical applications, a tradeoff between the target misalignment range, power variation, maximum primary current, and power losses should be considered to select the number of switching frequencies.

B. Comparison to Previous Topologies

Table III compares the capabilities of key prior solutions. In [31], an S-S topology uses frequency control method 2 to compensate misalignment. Although this method has the lowest component count, device and component ratings are higher and system efficiency drops rapidly because primary current and reactive power increase as the coupling coefficient decreases. A single-frequency topology based on X-type compensation was used in [27], but the primary current and power variation increase as coupling coefficient decreases, which limits the ability to extend the misalignment range. Compared to [27], the proposed method achieves a wider misalignment range, a narrower primary current range, and lower power variation with only three additional passive components. The system in [29] combines series and *LCC* compensation circuits, but the four-coil structure only achieves *x* and *z*-axis misalignment tolerance. The proposed method has the same component count as in [29], but can achieve three-dimensional misalignment tolerance. The reconfigurable topology proposed in [28] uses extra ac switches to change the equivalent compensation, but power device ratings and isolation challenges linked to these switches limit the ability to scale this approach to high power. The proposed method replaces extra switches and controllers with additional passive components and keeps component and device ratings relatively low, which benefits high-power applications. The approach in [28] is not able to extend the misalignment range while enforcing limits on power variation.

The proposed approach offers several advantages. Misalignment is supported in all directions. Since there is a single output power port, it is suitable for scaling to high power. With additional resonant tanks, operation can employ multiple discrete frequencies to extend the coupling range. The characteristics can be determined in advance to support straightforward open-loop frequency selection. The added resonant tanks will introduce additional inductors, which will increase system volume, but this could be a valid tradeoff as power levels increase. In future work, integration of compensation inductors with the coil will be explored. Magnetic integration has the promise to enhance system power density.

VI. CONCLUSION

This article proposes a primary detuned multifrequency compensation circuit and switching frequency operating method to extend IPT system misalignment tolerance with limited power variation. With multiple resonant frequencies, multiple intersecting power versus coupling coefficient curves at different switching frequencies are constructed. The analysis showed that power variation is linked directly to coupling coefficient range, nearly independent of other parameters. The proposed approach circumvents this characteristic by using multiple switching frequencies to extend the misalignment range with constrained power variation. Compared to single-frequency compensation,

primary current and reactive power at low coupling can be improved and power variation can be reduced substantially. In the test example, two-frequency and three-frequency circuits were selected to verify the analysis. The output power changed by less than 10% over a coupling coefficient range from 0.14 to 0.35 for two-frequency compensation, whereas for three-frequency compensation, the power change was about 6.7% over the same coupling range. In the test system, the coupling range corresponds to x-axis misalignment of up to 360 mm, y-axis misalignment of up to 135 mm, and z-axis gaps from 150 to 260 mm.

A 1.5 kW prototype IPT system has been built to demonstrate the feasibility and performance of the proposed approach. The system can maintain ZVS over the allowed range of coupling coefficients. At the maximum coupling coefficient, peak efficiency of two-frequency compensation is 94.6%, and efficiency exceeds 86% over the entire allowed coupling range. For three-frequency compensation, efficiency ranges from 85.7% to 94.1% over the entire coupling range.

REFERENCES

[1] J. Huh, S. W. Lee, W. Y. Lee, G. H. Cho, and C. T. Rim, "Narrow-width inductive power transfer system for online electrical vehicles," *IEEE Trans. Power Electron.*, vol. 26, no. 12, pp. 3666–3679, Dec. 2011.

[2] S. Y. R. Hui, W. Zhong, and C. K. Lee, "A critical review of recent progress in mid-range wireless power transfer," *IEEE Trans. Power Electron.*, vol. 29, no. 9, pp. 4500–4511, Sep. 2014.

[3] G. A. Covic and J. T. Boys, "Modern trends in inductive power transfer for transportation applications," *IEEE J. Emerg. Sel. Topics Power Electron.*, vol. 1, no. 1, pp. 28–41, Mar. 2013.

[4] C. Mi, G. Buja, S. Y. Choi, and C. T. Rim, "Modern advances in wireless power transfer systems for roadway powered electric vehicles," *IEEE Trans. Ind. Electron.*, vol. 63, no. 10, pp. 6533–6545, Oct. 2016.

[5] H. Feng, R. Tavakoli, O. C. Onar, and Z. Pantic, "Advances in high-power wireless charging systems: Overview and design considerations," *IEEE Trans. Transp. Electrific.*, vol. 6, no. 3, pp. 886–919, Sep. 2020.

[6] G. Guidi, J. A. Suul, F. Jenset, and I. Sorfonn, "Wireless charging for ships: High-power inductive charging for battery electric and plug-in hybrid vessels," *IEEE Electrific. Mag.*, vol. 5, no. 3, pp. 22–32, Sep. 2017.

[7] H. Feng, T. Cai, S. Duan, X. Zhang, H. Hu, and J. Niu, "A dual-side-detuned series–series compensated resonant converter for wide charging region in a wireless power transfer system," *IEEE Trans. Ind. Electron.*, vol. 65, no. 3, pp. 2177–2188, Mar. 2018.

[8] F. Liu, Y. Yang, Z. Ding, X. Chen, and R. M. Kennel, "A multi-frequency superposition methodology to achieve high efficiency and targeted power distribution for a multi-load MCR WPT system," *IEEE Trans. Power Electron.*, vol. 33, no. 10, pp. 9005–9016, Oct. 2018.

[9] D. Ahn and P. P. Mercier, "Wireless power transfer with concurrent 200-kHz and 6.78-MHz operation in a single-transmitter device," *IEEE Trans. Power Electron.*, vol. 31, no. 7, pp. 5018–5029, Jul. 2016.

[10] Y. Xiao, C. Liu, Y. Huang, and S. Liu, "Concurrent wireless power transfer to multiple receivers with additional resonant frequencies and reduced power switches," *IEEE Trans. Ind. Electron.*, vol. 67, no. 11, pp. 9292–9301, Nov. 2020.

[11] C. Zhao and D. Costinett, "GaN-based dual-mode wireless power transfer using multi-frequency programmed pulse width modulation," *IEEE Trans. Ind. Electron.*, vol. 64, no. 11, pp. 9165–9176, Nov. 2017.

[12] C. Xia, N. Wei, H. Zhang, S. Zhao, Z. Li, and Z. Liao, "Multifrequency and multiload MCR-WPT system using hybrid modulation waves SPWM control method," *IEEE Trans. Power Electron.*, vol. 36, no. 11, pp. 12400–12412, Nov. 2021.

[13] W. Zhong and S. Y. R. Hui, "Auxiliary circuits for power flow control in multifrequency wireless power transfer systems with multiple receivers," *IEEE Trans. Power Electron.*, vol. 30, no. 10, pp. 5902–5910, Oct. 2015.

[14] Y. Zhang, T. Lu, Z. Zhao, F. He, K. Chen, and L. Yuan, "Selective wireless power transfer to multiple loads using receivers of different resonant frequencies," *IEEE Trans. Power Electron.*, vol. 30, no. 11, pp. 6001–6005, Nov. 2015.

[15] X. Zhang, F. Liu, and T. Mei, "Multifrequency phase-shifted control for multiphase multiload MCR WPT system to achieve targeted power distribution and high misalignment tolerance," *IEEE Trans. Power Electron.*, vol. 36, no. 1, pp. 991–1003, Jan. 2021.

[16] Z. Liu, M. Su, Q. Zhu, L. Zhao, and A. P. Hu, "A dual frequency tuning method for improved coupling tolerance of wireless power transfer system," *IEEE Trans. Power Electron.*, vol. 36, no. 7, pp. 7360–7365, Jul. 2021.

[17] M. Budhia, G. Covic, and J. Boys, "A new IPT magnetic coupler for electric vehicle charging systems," in *Proc. IEEE Annu. Conf. Ind. Electron. Soc.*, Nov. 2010, pp. 2487–2492.

[18] M. Budhia, J. Boys, G. Covic, and C.-Y. Huang, "Development of a single-sided flux magnetic coupler for electric vehicle IPT charging systems," *IEEE Trans. Ind. Electron.*, vol. 60, no. 1, pp. 318–328, Jan. 2013.

[19] G. A. J. Elliott, S. Raabe, G. A. Covic, and J. T. Boys, "Multiphase pickups for large lateral tolerance contactless power-transfer systems," *IEEE Trans. Ind. Electron.*, vol. 57, no. 5, pp. 1590–1598, May 2010.

[20] A. Zaheer, G. A. Covic, and D. Kacprzak, "A bipolar pad in a 10-kHz 300-W distributed IPT system for AGV applications," *IEEE Trans. Ind. Electron.*, vol. 61, no. 7, pp. 3288–3301, Jul. 2014.

[21] M. Budhia, G. A. Covic, and J. T. Boys, "Design and optimization of circular magnetic structures for lumped inductive power transfer systems," *IEEE Trans. Power Electron.*, vol. 26, no. 11, pp. 3096–3018, Nov. 2011.

[22] Y. Wang, P. Gu, Y. Yao, and D. Xu, "Analysis and design of cubic magnetic coupler for high distance-to-diameter ratio IPT systems," *IEEE Trans. Ind. Electron.*, vol. 69, no. 1, pp. 409–419, Jan. 2022.

[23] R. Mai, B. Yang, Y. Chen, N. Yang, Z. He, and S. Gao, "A misalignment tolerant IPT system with intermediate coils for constant-current-output," *IEEE Trans. Power Electron.*, vol. 34, no. 8, pp. 7151–7155, Aug. 2019.

[24] F. Lu, H. Zhang, H. Hofmann, W. Su, and C. Mi, "A dual-coupled *LCC*-compensated IPT system with a compact magnetic coupler," *IEEE Trans. Power Electron.*, vol. 33, no. 7, pp. 6391–6402, Jul. 2018.

[25] Y. Chen, R. Mai, Y. Zhang, M. Li, and Z. He, "Improving misalignment tolerance for IPT system using a third-coil," *IEEE Trans. Power Electron.*, vol. 34, no. 4, pp. 3009–3013, Apr. 2019.

[26] J. Zhao, T. Cai, S. Duan, H. Feng, C. Chen, and X. Zhang, "A general design method of primary compensation network for dynamic WPT system maintaining stable transmission power," *IEEE Trans. Power Electron.*, vol. 31, no. 12, pp. 8343–8358, Dec. 2016.

[27] H. Feng, A. Dayerizadeh, and S. M. Lukic, "A coupling-insensitive X-type IPT system for high position tolerance," *IEEE Trans. Ind. Electron.*, vol. 68, no. 8, pp. 6917–6926, Aug. 2021.

[28] Y. Chen et al., "Reconfigurable topology for IPT system maintaining stable transmission power over large coupling variation," *IEEE Trans. Power Electron.*, vol. 35, no. 5, pp. 4915–4924, May 2020.

[29] L. Zhao, D. J. Thrimawithana, U. K. Madawala, A. P. Hu, and C. C. Mi, "A misalignment tolerant series-hybrid wireless EV charging system with integrated magnetics," *IEEE Trans. Power Electron.*, vol. 34, no. 2, pp. 1276–1285, Feb. 2019.

[30] Y. Chen, B. Yang, Z. H. Kou, Z. He, G. Cao, and R. Mai, "Hybrid and reconfigurable IPT systems with high-misalignment tolerance for constant current and constant voltage battery charging," *IEEE Trans. Power Electron.*, vol. 33, no. 10, pp. 8259–8269, Oct. 2018.

[31] E. Gati, G. Kampitsis, and S. Manias, "Variable frequency controller for inductive power transfer in dynamic conditions," *IEEE Trans. Power Electron.*, vol. 32, no. 2, pp. 1684–1696, Feb. 2017.

[32] C. Zheng et al., "High-efficiency contactless power transfer system for electric vehicle battery charging application," *IEEE J. Emerg. Sel. Topics Power Electron.*, vol. 3, no. 1, pp. 65–74, Mar. 2015.

[33] T. Diekhans and R. W. D. Doncker, "A dual-side controlled inductive power transfer system optimized for large coupling factor variations and partial load," *IEEE Trans. Power Electron.*, vol. 30, no. 11, pp. 6320–6328, Nov. 2015.

[34] Q. Chen, S. C. Wong, C. K. Tse, and X. Ruan, "Analysis design and control of a transcutaneous power regulator for artificial hearts," *IEEE Trans. Biomed. Circuits Syst.*, vol. 3, no. 1, pp. 23–31, Feb. 2009.

[35] C.-S. Wang, G. A. Covic, and O. H. Stielau, "Power transfer capability and bifurcation phenomena of loosely coupled inductive power transfer systems," *IEEE Trans. Ind. Electron.*, vol. 51, no. 1, pp. 148–157, Feb. 2004.

[36] P. T. Krein, *Elements of Power Electronics*, Int. 2nd ed. New York, NY, USA: Oxford Univ. Press, 2016, pp. 400–406.

[37] N. X. Bac, D. M. Vilathgamuwa, and U. K. Madawala, "A SiC-based matrix converter topology for inductive power transfer system," *IEEE Trans. Power Electron.*, vol. 29, no. 8, pp. 4029–4038, Aug. 2014.

Zirui Yao (Student Member, IEEE) received the B.S. degree in electrical engineering from South China University of Technology, Guangzhou, China, in 2018. He is currently working toward the Ph.D. degree in electrical engineering with Zhejiang University, Hangzhou, China.

His research interests include inductive power transfer and resonant converters.

Shiying Luo received the B.S. degree in electrical engineering and automation from Harbin Institute of Technology, Harbin, China, in 2019. He is currently working toward the Ph.D. degree in electrical engineering with Zhejiang University, Hangzhou, China.

His research interests include inductive power transfer and resonant converters.

Zhuhaobo Zhang (Student Member, IEEE) received the B.S. and Ph.D. degrees in electrical engineering from Zhejiang University, Hangzhou, China, in 2017 and 2022, respectively.

His research interests include wireless power transfer, resonant converters, and electric vehicle charging systems.

Guanxi Li received the B.S. and Ph.D. degrees in electrical engineering from Zhejiang University, Hangzhou, China, in 2016 and 2022, respectively.

His current research focuses on wireless power transfer, including the research of compensation topology and IPT pads.

Xuan Wei (Student Member, IEEE) received the B.S. degree in electrical engineering, in 2018, from Zhejiang University, Hangzhou, China, where she is currently working toward the Ph.D. degree in electrical engineering.

Her research interests include capacitive power transfer and resonant converters.

Xiangwei Shen received the B.S. degree in electrical engineering, in 2020, from Zhejiang University, Hangzhou, China, where he is currently working toward the Ph.D. degree in electrical engineering.

His research interests include capacitive power transfer, resonant converters, and dc–dc converters.

Ni Zhang received the B.S. and M.S. degrees in electrical engineering, in 1992 and 1997, respectively, and Ph.D. degree in control engineering in 2002, all from Zhejiang University, Hangzhou, China.

From 1992 to 1994, she was with the Department of Electrical Engineering, Zhejiang University. From April 2016 to April 2017, she was a Visiting Scholar with North Carolina State University. In 2002, she joined Zhejiang University of Technology, Hangzhou, China, where she is currently an Associate Professor. Her research interests include deep learning applications in power electronics, deep learning based medical image analysis, and switched systems.

Philip T. Krein (Fellow, IEEE) received the B.S. degree in electrical engineering and the A.B. degree in economics and business from Lafayette College, Easton, PA, USA, in 1978, and the M.S. and Ph.D. degrees in electrical engineering from the University of Illinois at Urbana–Champaign, Champaign, IL, USA, in 1980 and 1982, respectively.

He was an Engineer with Tektronix, Beaverton, OR, USA, and then returned to the University of Illinois at Urbana–Champaign. From 1997 to 1998, he was a Senior Fulbright Scholar with the University of Surrey, Guildford, U.K. From 2003 to 2014, he was a Founder and Director of SolarBridge Technologies, Inc., Austin, TX, USA, a Developer of ac photovoltaic panels. From 2016 to 2020, he was an Executive Dean of the Zhejiang University/University of Illinois at Urbana–Champaign Institute, Haining, China. He holds the Grainger Endowed Chair Emeritus in Electric Machinery and Electromechanics with the University of Illinois at Urbana–Champaign. He holds 42 U.S. patents. His research interests include all aspects of power electronics, machines, drives, and electric transportation, with emphasis on nonlinear control approaches.

Dr. Krein was the recipient of the IEEE William E. Newell Power Electronics Award in 2003 and the IEEE Transportation Technologies Award in 2021. He is a Past President of the IEEE Power Electronics Society, a past member of the IEEE Board of Directors, and a Past Chair of the IEEE Transportation Electrification Community. He is an Associate Editor for the IEEE OPEN JOURNAL OF POWER ELECTRONICS. He is a Registered Professional Engineer in Illinois and Oregon, a Fellow of the U.S. National Academy of Inventors, and a member of the U.S. National Academy of Engineering.

Hao Ma (Senior Member, IEEE) received the B.S., M.S., and Ph.D. degrees in electrical engineering from Zhejiang University, Hangzhou, China, in 1991, 1994, and 1997, respectively.

Since 1997, he has been a Lecturer, Associate Professor, and Professor with Zhejiang University. From September 2007 to September 2008, he was a Delta Visiting Scholar with the North Carolina State University. He is the Vice Dean of the Zhejiang University/University of Illinois at Urbana-Champaign Institute, Haining, China. He has authored two books and has authored or coauthored more than 300 technical papers. His research interests include advanced control in power electronics, wireless power transfer, fault diagnosis of power electronic circuits and systems, and application of power electronics.

Dr. Ma is currently the Vice President of China Power Supply Society. He was the Associate Editor for the IEEE JOURNAL OF EMERGING AND SELECTED TOPICS IN POWER ELECTRONICS and *Journal of Power Electronics*. He was the AdCom Member of the IEEE Industrial Electronics Society, the Technical Program Chair of the IEEE International Symposium on Industrial Electronics 2012, IEEE International Power Electronics and Application Conference and Exposition 2014, IEEE International Power Electronics and Application Conference and Exposition 2018, and IEEE International Power Electronics and Application Conference and Exposition 2022.